# Direct-Drive, Cryogenic Target Implosions on OMEGA

## Introduction

Thermonuclear ignition via direct-drive, laser-driven, inertial confinement fusion[1] (ICF) will be accomplished by the near-uniform illumination of spherical cryogenic deuterium–tritium (DT) fuel-bearing capsules with high-power laser beams. Achieving thermonuclear ignition and gain will require symmetric compression of the DT-fuel hot spot to high areal densities (~0.3 g/cm$^2$) with a temperature of ~10 keV. The baseline target consists of either a pure cryogenic DT layer formed on the inside of a thin plastic shell[2] or a DT-filled foam shell.[3] Target imperfections and laser illumination nonuniformities lead to Rayleigh–Taylor unstable growth of fuel-layer perturbations during the implosion and must be minimized. The minimum energy required for ignition scales as $\sim\alpha^{1.8}$ (Refs. 4–6), where $\alpha$ is the fuel adiabat, the ratio of the local pressure to the Fermi-degenerate pressure. It has been shown that the ablation velocity, the main contributor to the stabilization of Rayleigh–Taylor unstable growth, scales as $\sim\alpha^{0.6}$ (Ref. 4). Traditionally, direct-drive ICF has had to balance target performance and stability by a careful choice of the target adiabat. This task has been made easier with the application of adiabat shaping.[7] The ablation region is placed on a high adiabat for stability while maintaining the main fuel layer on a low adiabat, preserving compressibility for good target performance.

The experiments described in this work were performed on LLE's 60-beam, 30-kJ UV OMEGA laser system.[8] The three major requirements to achieve ignition-scaled conditions in the fuel have been met: (1) near-uniform cryogenic layers, (2) near-uniform laser illumination, and (3) a high-contrast pulse shape maintaining the fuel layer on a low adiabat ($\alpha \sim 4$). The resulting high fuel areal densities ($\rho R \sim 100$ mg/cm$^2$), ion temperature ($kT_i \sim 2$ to 3 keV), and fusion yield [~20% of predicted by one-dimensional (1-D) simulations and in agreement with two-dimensional (2-D) simulations] give increasing confidence to the direct-drive approach to ICF ignition.

This work describes recent progress in direct-drive, cryogenic target implosions on OMEGA. The following sections (1) describe the experimental conditions and observations, (2) compare the observations with 2-D numerical simulations, and (3) present our conclusions.

## Experiments

This section describes the experimental conditions, including target and laser performance, and the primary experimental observations.

### 1. Targets

The targets used in these experiments were $D_2$-filled, deuterated, strong GDP (a high-strength, glow-discharge polymer) shells with outer diameters of ~865 $\mu$m, shell thicknesses of ~3.7 to 4.0 $\mu$m, and a density of 1.09 g/cm$^3$. The shells were permeation filled with ~1000 atm of $D_2$ gas in the Fill/Transfer Station (FTS)[9] and then slowly cooled to below the triple point (18.7 K). The targets were then transported to a characterization station for layer formation and then to the OMEGA target chamber for implosion.

The formation of a near-uniform layer is accomplished in a layering sphere[9] using an IR laser tuned to the $D_2$-ice absorption band at a wavelength of 3.16 $\mu$m. The residual inner-ice-surface nonuniformities, after careful layer preparation, are determined using the shadowgraphic technique described in Stoeckl *et al.*[10] and shown in Fig. 102.21. This technique has been extended to map the inner surface of the ice layer in 3-D by combining layer-thickness measurements from multiple views (48 typically, consisting of 24 orthogonal pairs). In addition to the inner-ice-surface roughness, the outer-surface roughness of the CH shell is also determined. The mean inner-ice roughness for the target experiments included in this work was 5 $\mu$m (rms) with the best being 1.3 $\mu$m. Three-dimensional (3-D) reconstructions of the ice layer from these multiple views were used as input to the 2-D hydrodynamic simulations described in **Comparison of Experimental Results and 2-D Simulations** (p. 82).

The standard deviation of the mean layer thickness from individual views is typically $\lesssim 2$ $\mu$m. However, there are other

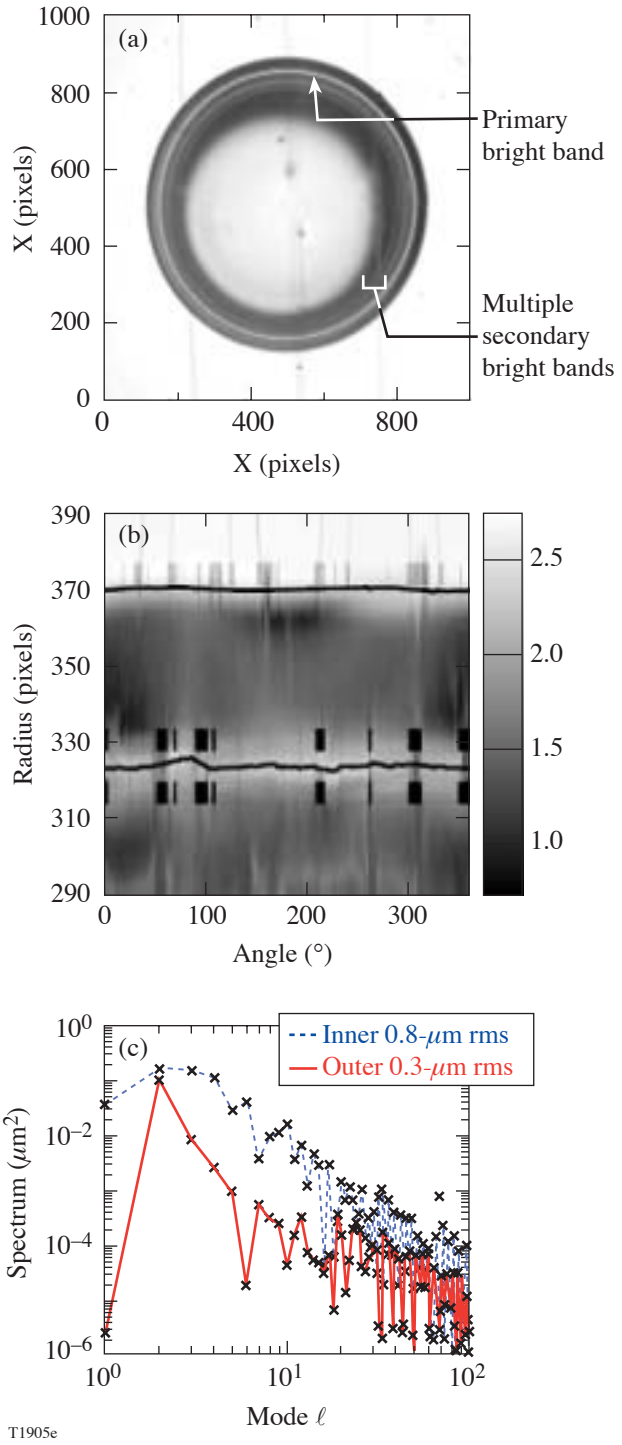


Figure 102.21
Cryogenic target layer characterization. (a) A single shadowgraph, (b) layer-thickness measurements, and (c) resultant mode spectrum.

ways to characterize the errors of the ice-layer nonuniformity. For example, the ice layer for shot 35713 had a 4.2-$\mu$m mean rms, predominately in the four lowest $\ell$ modes. Based on the 3-D reconstruction of the ice layer, a peak-to-valley of $\pm 10$ $\mu$m existed over ~1% of the surface. These larger variations will likely affect target performance to a greater degree than represented by the standard deviation of the mean of the individual measurements. An effort is underway to more accurately determine the mean ice-roughness error and its impact on target performance and simulations.

## 2. Laser System Conditions

Cryogenic capsules were imploded with pulse shapes ranging from a high-adiabat ($\alpha \sim 25$), 23-kJ, 1-ns square pulse to a low-adiabat ($\alpha \sim 4$), 17-kJ, 2.5-ns shaped pulse. The fuel adiabat at the end of the acceleration phase is determined by using the pulse shape, as measured by a high-bandwidth streak camera,[11] as input to the 1-D hydrocode *LILAC*.[12] Full beam smoothing, including distributed phase plates (DPP's),[13] polarization smoothing with distributed polarization rotators (DPR's),[14] and 2-D, single-color-cycle, 1-THz smoothing by spectral dispersion (SSD),[15] was used for these experiments. Recent experiments ($\alpha \sim 4$) were performed with a new set of DPP's[16] with a 95% enclosed energy diameter of 865 $\mu$m and a "super-Gaussian" order $n = 3.7$. The new DPP's reduce the need to use enhanced fluence balance.[17] Beam mispointing is reduced from an average of ~20-$\mu$m rms to an average of ~10-$\mu$m rms by active repointing requiring two pointing shots.[16,17] These combined effects have reduced the long-wavelength nonuniformities of the laser system from ~3% to ~1.3%. This condition was applied to all $\alpha \sim 4$ implosions in this work. The largest contribution to the long-wavelength nonuniformities is the location of the target with respect to the center of the target chamber (TCC offset) at shot time.

## 3. Absorption Measurements

The scattered light was measured by calorimeters in two full-aperture-backscatter stations (FABS's). These calorimeters sample the light backscattered through two OMEGA focusing lenses. Extensive 2-D ray-tracing simulations using 1-D hydrodynamic code predictions for the time-varying plasma density and temperature profiles have shown that the scattered light variations around the target are within ~3% of perfect uniformity. Spot measurements with calorimeters between the OMEGA focusing lens positions have confirmed these predictions. Nevertheless, random shot-to-shot fluctuations in the various calorimeter measurements can be as high as 7% rms per shot. These fluctuations are thought to be due to target centering and subtle beam-pointing issues. In contrast,

the shot-to-shot reproducibility of the average calorimeter reading is typically within 2% to 3%, inspiring confidence in the validity of the average scattered-light measurements. Since the long-term calibration stability of the scattered-light calorimeters between the focusing lenses is difficult to ascertain, we use only scattered-light energies measured at the two FABS's and extrapolate them to $4\pi$. These data yield a good measure for the total absorbed energy.

Reliable measurements of absorbed energy in spherical target implosions are essential for quantitative comparison with hydrodynamic code simulations. The absorption predicted by these codes is based primarily on 2-D ray tracing and inverse bremsstrahlung absorption and depends sensitively on the electron thermal transport. The latter is typically modeled using flux-limited diffusion.[18,19] A flux limiter $f = 0.06$ was used for all simulations in this work.

Figure 102.22 shows the fractional difference of the measured absorption from *LILAC* predictions for a series of cryogenic implosions with the pulse shapes shown as insets. Error bars represent the difference of the two FABS measurements. The agreement between the measurements and the 1-D *LILAC* predictions is excellent (horizontal dashed lines in Fig. 102.22) when averaged over all shots. We have also made time-resolved scattered-light measurements (and, consequently, time-resolved absorption measurements) that are in equally good agreement over the entire pulse shape for all of the pulse shapes.[20]

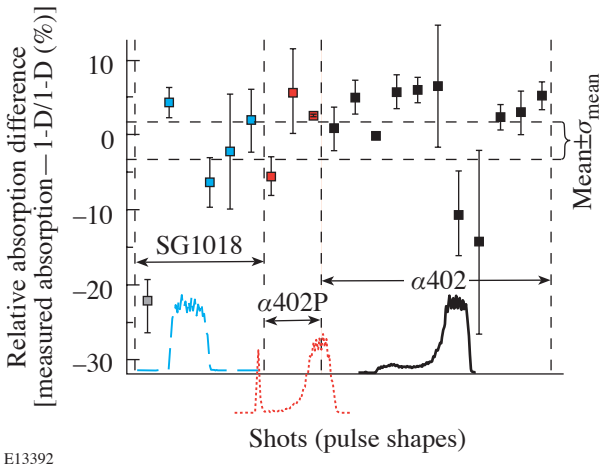


Figure 102.22
Absorption fraction measurements shown as percent variation from 1-D predicted value.

Determination of the fuel adiabat depends on the detailed time history of the absorbed energy, requiring precision measurement of the laser pulse shape. Using P510 streak cameras[11] with a demonstrated bandwidth of ~20 GHz in the UV in selected channels, the simulations are provided with pulse shapes that include an initial low-intensity rise of ~40 ps/decade for all pulse shapes. These rise times were measured using 1-ns square pulses best suited for this purpose. The same pulse switching provides the initial rise for all other pulse shapes. Details of the initial rise are of importance to simulations. With these inputs, optimum zoning strategies were developed for the *LILAC* simulations that led to improved absorption calculations[7] in the leading edge of the strongly shaped $\alpha$401, $\alpha$402, and $\alpha$402P (with picket) pulses. All of these improvements have led to better agreement between the measured and simulated time-integrated and time-resolved absorption fractions, as well as improved estimates for the fuel adiabat during the implosion phase. Thus, previously predicted $\alpha \sim 4$ pulses were found to produce slightly higher calculated adiabats ($\alpha \sim 6$). New pulse shapes, incorporating better design of the leading edge, have been incorporated into current OMEGA experiments.

## 4. Fusion Yield

The fusion reaction rate for these experiments is determined by the neutron temporal diagnostic (NTD),[21] with the absolute rate obtained by normalizing with the neutron yield. Figure 102.23 shows the NTD measured and simulated neutron rate for a low-adiabat ($\alpha \sim 4$) implosion. The duration and peak time are seen to fall within the absolute measurement uncertainty (±0.1 ns). The integrated yield for this implosion was $1.6 \times 10^{10}$, while the *LILAC* prediction was $9.1 \times 10^{10}$ [yield over calculated (YOC) = 18%]. The coincidence of the measured and predicted peak burn times confirms the observations from the absorption measurements that the simulations are correctly predicting the absorption and hydrodynamic coupling in cryogenic targets.

## 5. Fuel Areal Density

The total fuel areal density in cryogenic $D_2$ implosions is inferred from the energy loss of secondary protons from the $D^3He$ reaction. The secondary proton spectrum at birth is well defined by the kinematics of the $D^3He$ reaction so that the average energy of the protons emerging from the dense fuel depends on the total burn-averaged areal density $\langle \rho R \rangle_n$. Wedged-range-filter spectrometers (WRF's)[22] measure the secondary proton spectrum along multiple lines of sight (generally four to six). These individual measures of the $\rho R_n$ are averaged to obtain the reported $\langle \rho R \rangle_n$. The error associated with each

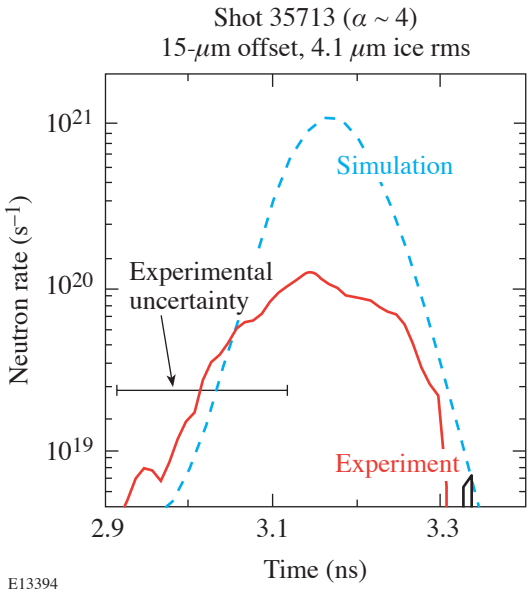


Figure 102.23
NTD measurement of the fusion reaction rate for an $\alpha \sim 4$ cryogenic target implosion (shot 35713). The 1-D simulated fusion rate is also plotted.

individual measure is approximately 5% (typically a 150-keV uncertainty out of a 3-MeV energy loss). However, the variation among the individual measurements is often quite large due to low-mode variations in the initial ice thickness and drive symmetry. The dominant factor in the drive asymmetry is the location of the capsule with respect to chamber center at shot time (the TCC offset discussed above).

Figure 102.24 shows the correlation between the experimentally inferred $\langle \rho R \rangle_n$ and the value of $\langle \rho R \rangle_n$ predicted by the 1-D hydrocode *LILAC* for all cryogenic implosions in which the offset from TCC was <60 $\mu$m and the inner-ice-layer rms roughness was <6 $\mu$m. The solid circles near 50 mg/cm$^2$ represent high-adiabat implosions ($\alpha \sim 25$) driven by a 1-ns square pulse (see Fig. 102.22) and show near 1-D performance in the assembly of the fuel (typically, the primary neutron yields are 50% to 70% of 1-D). The open circles represent low-adiabat implosions using a high-contrast pulse shape similar to the one shown in Fig. 102.22. Although designed to put the fuel shell on an adiabat of 4, the actual shape of the drive pulse delivered to the capsules varied from shot to shot such that the calculated adiabat ranged from ~4 to just over 6. In a few cases, the calculated adiabat ranged between 6 and 12. Therefore, the points are labeled as "mid-$\alpha$" and "$\alpha \sim 4$ to 6" [a subset of these implosions is discussed later in **Comparison of Experimental Results and 2-D Simulations** (p. 82)]. The key feature to note is that as the adiabat of the fuel decreases, the deviation of the experimentally inferred $\langle \rho R \rangle_n$ from 1-D performance increases. This discrepancy is expected and discussed further in **Comparison of Experimental Results and 2-D Simulations** (p. 82).

The drive pulses for the most recent implosions (shots 37967 and 37968) were carefully tuned to obtain the desired adiabat in the fuel. These two points are labeled as "$\alpha = 3.5$ to 3.8." The $\langle \rho R \rangle_n$ for shot 37968 was 98±22 mg/cm$^2$. The error here represents the standard deviation of the individual measurements (seven for this shot) and suggests a significant offset from TCC at shot time (the standard deviation is typically much larger than the errors associated with the individual measurements). For this shot, the measured offset was ~40 $\mu$m. The error bar is considerably smaller for shot 35713 and consistent with the much smaller offset at shot time, 15 $\mu$m. This confirms that the variation among the individual measurements is dominated by the offset from TCC at shot time.

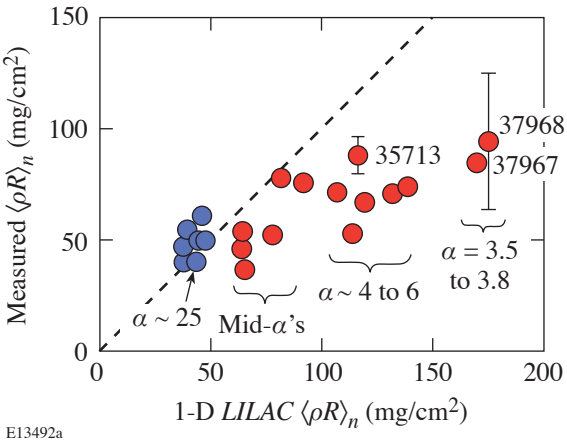


Figure 102.24
Measured $\langle \rho R \rangle_n$ as function of 1-D predicted value. The range of fuel adiabats is also indicated.

6. Stagnation

Peak density occurs in these implosions after the time of peak neutron production. Recent works[23,24] have shown that the time history of the fuel $\rho R$ can be inferred from the combined measurements of the proton spectrum and the reaction rate history. The fuel $\rho R$ increases until final stagnation, when the bulk of the fuel is heated to a lower temperature than the hot

core. At this point, the x-ray flux increases dramatically, allowing a diagnosis of stagnation by x-ray imaging. Figure 102.25 shows a pair of quasi-monochromatic x-ray images from a grating-dispersed Kirkpatrick–Baez (KB) microscope[25] [Fig. 102.25(a)] and an x-ray framing camera (XRFC) filtered to be sensitive to x rays in the range of 4 to 5 keV [Fig. 102.25(b)]. The KB microscope is time integrating, has a resolution of ~3 $\mu$m, and is dispersed by a transmission grating that convolves space and spectrum in the spectral direction.[25] The stagnation-region size as a function of mean wavelength can be measured in the perpendicular direction. The radial profile of this emission at 4 keV is shown in Fig. 102.25(c) along with the azimuthal average lineout from the XRFC image (frame closest to peak x-ray emission within ±50 ps, and within a 50-ps time window). These are compared with the simulated time-integrated emission profile from a *LILAC* postprocessor. The good agreement between both measurements and the simulated profile indicates that the fuel-stagnation core size is close to the 1-D prediction. The absolute flux and slope of the continuum determined from the grating-dispersed KB image [Fig. 102.25(d)] also show close agreement with the 1-D postprocessor prediction. The inferred stagnation electron temperature is $kT_e$ = 1.3 keV (averaged over the time of the x-ray emission).

### Comparison of Experimental Results and 2-D Simulations

The goal of the OMEGA cryogenic implosion program is to validate the predicted performance of low-adiabat, ignition-scaled implosions on OMEGA. The first set of experiments in this phase employs an $\alpha \sim 4$ pulse shape (shown as an inset in Fig. 102.22). Several $\alpha \leq 4$ implosions (see Fig. 102.24) were undertaken using the OMEGA laser; for brevity, only a single implosion (35713) will be described in detail.

The target was 870 $\mu$m in diameter with a 3.8-$\mu$m-thick GDP shell, a 95-$\mu$m-thick $D_2$-ice layer, and an interior-ice-surface roughness of 4.2 $\mu$m. The power spectrum for this surface, as shown in Fig. 102.26(a), is heavily weighted toward low-order modes. The capsule was ~15 $\mu$m from target chamber center at the beginning of the implosion. The experimental neutron yield for this implosion was $1.6 \times 10^{10}$, which represents the highest-ever experimental yield obtained from a cryogenic $\alpha \sim 4$ implosion (YOC ~ 18%). The ice-roughness spectrum from Fig. 102.26(a) and an initial 3.1%, $\ell$ = 1 illumination nonuniformity, due to the target offset, were used in a *DRACO* 2-D hydrodynamic simulation.[26] Laser imprint was modeled in these calculations with modes $\ell$ = 2 to 200. The simulated core can be seen in Fig. 102.26(b) to have

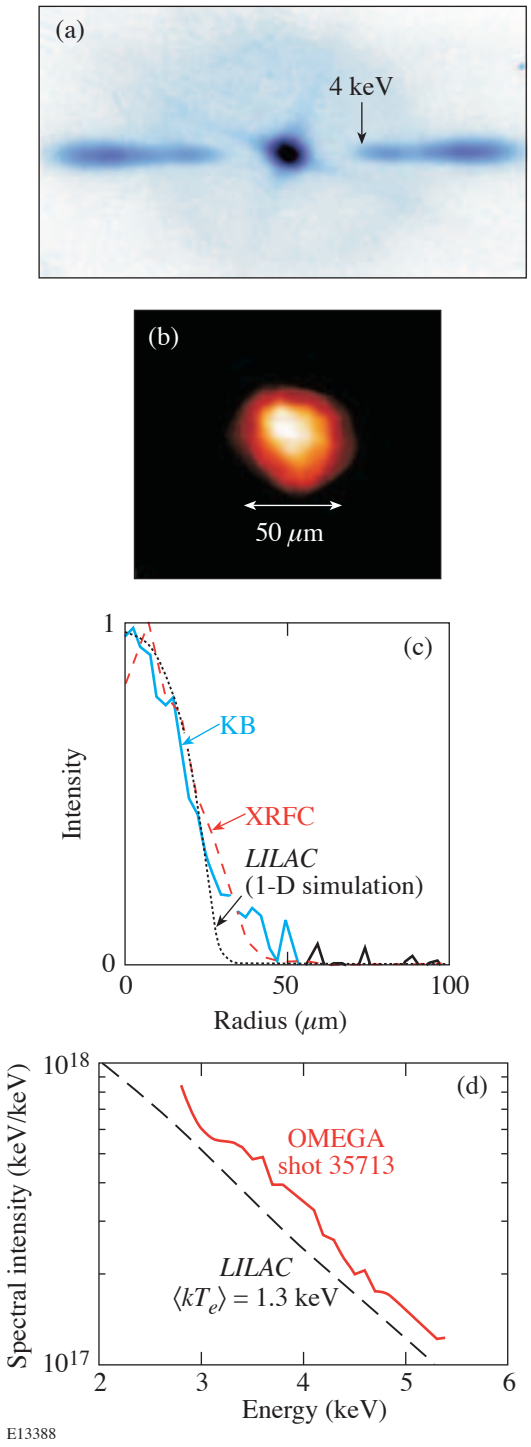


Figure 102.25
X-ray images of the fuel core at stagnation (shot 35713) from (a) a grating-dispersed KB and (b) an XRFC. (c) Radial profiles of images compared to 1-D prediction, and (d) absolute continuum x-ray spectrum (3 to 5 keV) obtained from a KB image of core emission compared to the 1-D prediction.

assembled slightly (~10 $\mu$m) off-axis due to the presence of the $\ell = 1$ component of the initial inner-ice roughness and target offset, resulting in a 2-D simulated neutron yield of $1.8 \times 10^{10}$. Additional measurements and simulations are given in Fig. 102.26(c). The core performance, however, is not dominated by the $\ell = 1$ perturbation, as has been the case with previous experiments, but is dominated by the presence of growing perturbations due to modes 6 to 10 from the illumination. The performance of this implosion was also seen to be somewhat sensitive to the presence of laser imprint, due to the stability characteristics of the $\alpha \sim 4$ pulse. While the core does not appear to be influenced by the high-frequency modes, the presence of these modes is observed in the overdense regions of the shell near the corona. Simulations without laser imprint resulted in ~20%- to 25%-higher neutron yields. The secondary-yield comparison also shows that the *DRACO* simulation is close to the experimental result. The simulated neutron-averaged areal density $\left[\langle \rho R \rangle_n (DRACO) = 101 \text{ mg/cm}^2\right]$ is close to the experimentally obtained value

$$\left[\langle \rho R \rangle_n (\text{expt.}) = 88 \pm 10 \text{ mg/cm}^2\right].$$

The angular variation of the simulation and the range of measured values are shown in Fig. 102.26(d).

It should be noted that the calculated and measured ion temperatures do not agree. The calculation of the ion temperature in the hydrocodes does not include the effect of the collective motion of the fuel. Furthermore, the calculation does not produce a thermally broadened neutron energy spectrum, which is what is used to experimentally infer the plasma ion temperature during the burn. This discrepancy will be addressed in the future.

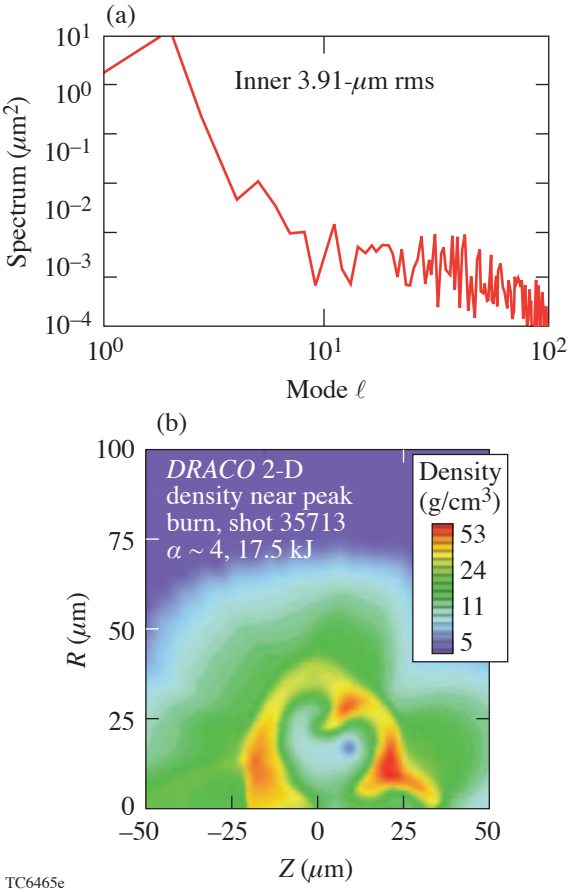


(c)

| | Expt. | 1-D | 2-D |
|---|---|---|---|
| $Y_{1n}$ | $1.6 \times 10^{10}$ | $9.1 \times 10^{10}$ | $1.8 \times 10^{10}$ |
| $Y_{2n}$ | $2.6 \times 10^{8}$ | $1.7 \times 10^{9}$ | $2.8 \times 10^{8}$ |
| $\langle \rho R \rangle$ (mg/cm$^2$) | 88 | 117 | 101 |
| $T_{ion}$ (keV) | 3.0 | 1.9 | 1.7 |

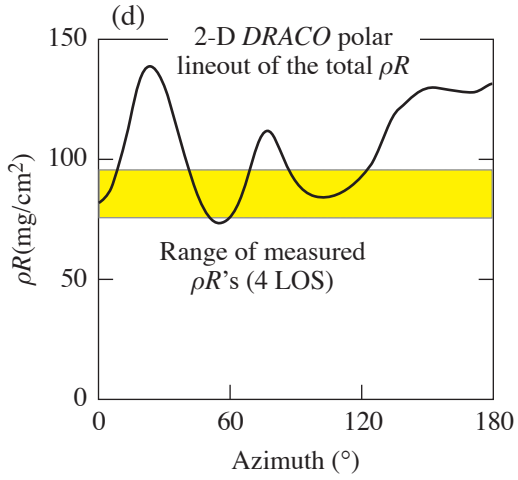


Figure 102.26
2-D *DRACO* simulation of shot 35713. (a) Spectrum of $D_2$-ice-surface roughness used as input, (b) isodensity contours at time of peak neutron-production rate, (c) table of measured and predicted primary and secondary yields, $\langle \rho R \rangle_n$, and ion temperature, and (d) angular variation of areal density from *DRACO* simulation with the range of measurements indicated by the shaded region.

Low-adiabat target performance has been previously presented[2] as a compilation of all perturbation sources using a sum-in-quadrature representation of each source's contribution to the roughness of the inner ice layer at the end of the acceleration phase of the implosion. The scaling parameter $\bar{\sigma}$ is defined as

$$\bar{\sigma}^2 = 0.06\sigma^2_{\ell(\ell<10)} + \sigma^2_{\ell(\ell>10)},$$

where $\sigma_\ell$ is the rms roughness computed over the indicated mode range. At this time in the implosion, this surface decouples from the ablation region. The effects of all major sources of perturbation leading to the initial seed of the deceleration-phase Rayleigh–Taylor (RT) instability have then been set. An example of the $\bar{\sigma}$ scaling determined from 2-D *DRACO* simulations is shown in Fig. 102.27, where a comparison is made between the NIF $\alpha = 3$ and OMEGA $\alpha = 4$ designs.

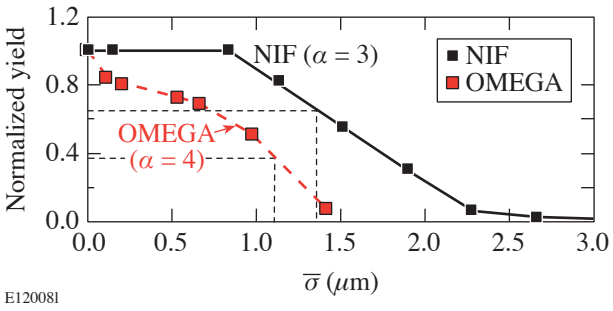


Figure 102.27
Comparison of the $\bar{\sigma}$ stability analysis for OMEGA $\alpha = 4$ and NIF $\alpha = 3$ designs. All values were determined with the hydrocode *DRACO*.

From Fig. 102.27 it can be seen that the OMEGA implosions are more sensitive to the higher values of $\bar{\sigma}$ than the NIF implosions. This is because the OMEGA targets have been energetically scaled from their NIF ignition counterparts. The physically smaller OMEGA targets are more sensitive than NIF targets when exposed to the same levels of nonuniformities. For identical values of $\bar{\sigma}$, the OMEGA implosions result in lower values of yield relative to 1-D simulations.

Using the $\bar{\sigma}$ scaling with yield allows an experimental validation of the numerical modeling of current OMEGA experiments. This lends credibility to the ability of these numerical models to predict ignition for direct-drive target designs on the NIF. Using current NIF specifications for the allowed levels of perturbations (imprint, power imbalance, and inner- and outer-surface roughness) results in a $\bar{\sigma}$ value of ~1.4 for the NIF capsule with a gain of ~30 (see McKenty *et al.*[2]). The corresponding OMEGA implosion would have a $\bar{\sigma}$ value of ~1.1 and a performance YOC of ~40%. These conditions are denoted as the dashed lines in Fig. 102.28, representing the performance of OMEGA implosions required for the validation of the ignition design.

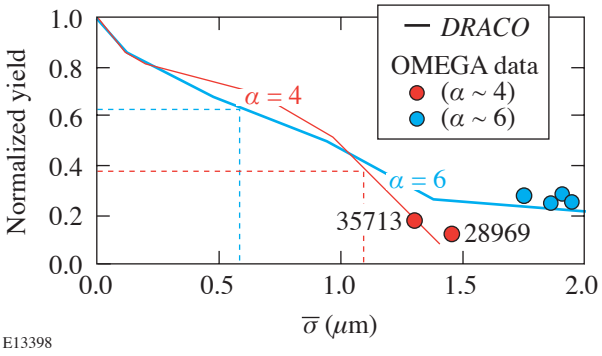


Figure 102.28
Comparison of *DRACO* predictions of yield reduction as a function of $\bar{\sigma}$ for $\alpha \sim 4$ and $\alpha \sim 6$ experiments on OMEGA.

Figure 102.28 illustrates the $\bar{\sigma}$ scaling for both the OMEGA $\alpha \sim 4$ and previous $\alpha \sim 6$ implosions. While it appears that $\bar{\sigma}$ scales the same for the $\alpha \sim 4$ and $\alpha \sim 6$ implosions, one must remember that $\bar{\sigma}$ represents the outcome of Rayleigh–Taylor growth of perturbation seeds during the acceleration phase of the implosion. Identical initial perturbations imposed during $\alpha \sim 4$ and $\alpha \sim 6$ target implosions will not result in the same $\bar{\sigma}$ value. The separate stability characteristics of the two implosions determine the final $\bar{\sigma}$ value for each target. As such, the $\alpha \sim 6$ implosions, due to their enhanced stability relative to the $\alpha \sim 4$ implosions, have resultant $\bar{\sigma}$ values that are lower than $\alpha \sim 4$ implosions with comparable initial conditions. The $\bar{\sigma}$ parameter (extracted from *DRACO* simulations) has been used to plot the experimental yield performance on the graph in Fig. 102.28 for recent OMEGA experiments. The experimental points are in good agreement with the $\bar{\sigma}$ scaling. As target-layer uniformity and OMEGA irradiation uniformity are improved, the $\alpha \sim 4$ implosion experiments are expected to approach the ~40% YOC goal.

Additional results obtained from all $\alpha \sim 6$ and $\alpha \sim 4$ implosions with ice quality better than 5-μm rms and target offset <42 μm are shown in Fig. 102.29. The YOC for the experimen-

tal data is compared with the trends of two series of *DRACO* simulations run with varying initial ice roughness for no offset and for a 30-$\mu$m offset from target chamber center. The effects of laser imprint are included in all of the *DRACO* simulations. The *DRACO* simulations are in good agreement with the YOC values and, therefore, explain yield reduction as due principally to the ice-layer roughness and target offset.

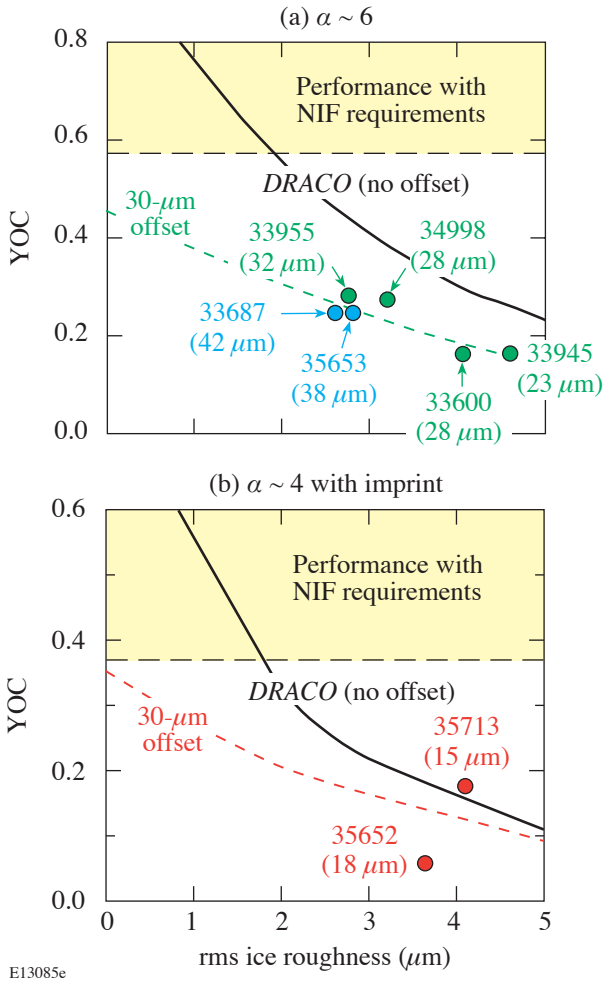


Figure 102.29
Comparison of YOC to *DRACO* predictions for (a) $\alpha \sim 6$ and (b) $\alpha \sim 4$ experiments on OMEGA as a function of ice roughness and target offset. Lower curves are *DRACO*-simulated YOC for a 30-$\mu$m target offset.

## Conclusions

In summary, recent cryogenic, $D_2$ direct-drive implosions on the OMEGA Laser System are showing good agreement with numerical simulations. Measurement and simulation of absorption agree closely (within ±2%), enabling the accurate design of pulse shapes that maintain the fuel on a calculated adiabat of as low as ~4. Areal densities of as high as ~100 mg/cm$^2$ for temperatures of ~2 to 3 keV result from implosions that have low ice roughness, low target offset, and low calculated fuel adiabat. Resulting fusion yields are well explained by 2-D simulations, and the expected reduction of yield from 1-D is currently limited by the ice roughness and target offset. Extrapolation to conditions on the NIF result in high gain (≳30), increasing confidence in the direct-drive approach to ICF ignition.

## ACKNOWLEDGMENT

The authors are extremely grateful to the staff of the Laboratory for Laser Energetics for their tireless dedication to the cryogenic implosion program and the operation of the OMEGA laser system. In particular, the authors would like to acknowledge the efforts of the Cryogenic Target Fabrication Group for the production of layered and characterized capsules on a regular schedule. This work was supported by the U. S. Department of Energy Office of Inertial Confinement Fusion under Cooperative Agreement No. DE-FC52-92SF19460, the University of Rochester, and the New York State Energy Research and Development Authority. The support of the DOE does not constitute an endorsement by the DOE of the views expressed in this article.

## REFERENCES

1. J. Nuckolls *et al.*, Nature **239**, 139 (1972).
2. P. W. McKenty, V. N. Goncharov, R. P. J. Town, S. Skupsky, R. Betti, and R. L. McCrory, Phys. Plasmas **8**, 2315 (2001).
3. S. Skupsky, R. Betti, T. J. B. Collins, V. N. Goncharov, D. R. Harding, R. L. McCrory, P. W. McKenty, D. D. Meyerhofer, and R. P. J. Town, in *Inertial Fusion Sciences and Applications 2001*, edited by K. Tanaka, D. D. Meyerhofer, and J. Meyer-ter-Vehn (Elsevier, Paris, 2002), pp. 240–245.
4. R. Betti, V. N. Goncharov, R. L. McCrory, and C. P. Verdon, Phys. Plasmas **5**, 1446 (1998).
5. M. C. Herrmann, M. Tabak, and J. D. Lindl, Nucl. Fusion **41**, 99 (2001).
6. J. Meyer-ter-Vehn, Nucl. Fusion **22**, 561 (1982).
7. V. N. Goncharov, J. P. Knauer, P. W. McKenty, P. B. Radha, T. C. Sangster, S. Skupsky, R. Betti, R. L. McCrory, and D. D. Meyerhofer, Phys. Plasmas **10**, 1906 (2003).
8. T. R. Boehly, D. L. Brown, R. S. Craxton, R. L. Keck, J. P. Knauer, J. H. Kelly, T. J. Kessler, S. A. Kumpan, S. J. Loucks, S. A. Letzring, F. J. Marshall, R. L. McCrory, S. F. B. Morse, W. Seka, J. M. Soures, and C. P. Verdon, Opt. Commun. **133**, 495 (1997).
9. Laboratory for Laser Energetics LLE Review **81**, 6, NTIS document No. DOE/SF/19460-335 (1999). Copies may be obtained from the National Technical Information Service, Springfield, VA 22161.
10. C. Stoeckl, C. Chiritescu, J. A. Delettrez, R. Epstein, V. Yu. Glebov, D. R. Harding, R. L. Keck, S. J. Loucks, L. D. Lund, R. L. McCrory, P. W. McKenty, F. J. Marshall, D. D. Meyerhofer, S. F. B. Morse, S. P. Regan, P. B. Radha, S. Roberts, T. C. Sangster, W. Seka, S. Skupsky,

V. A. Smalyuk, C. Sorce, J. M. Soures, R. P. J. Town, J. A. Frenje, C. K. Li, R. D. Petrasso, F. H. Séguin, K. Fletcher, S. Padalino, C. Freeman, N. Izumi, R. Lerche, and T. W. Phillips, Phys. Plasmas **9**, 2195 (2002).

11. W. R. Donaldson, R. Boni, R. L. Keck, and P. A. Jaanimagi, Rev. Sci. Instrum. **73**, 2606 (2002).

12. M. C. Richardson, P. W. McKenty, F. J. Marshall, C. P. Verdon, J. M. Soures, R. L. McCrory, O. Barnouin, R. S. Craxton, J. Delettrez, R. L. Hutchison, P. A. Jaanimagi, R. Keck, T. Kessler, H. Kim, S. A. Letzring, D. M. Roback, W. Seka, S. Skupsky, B. Yaakobi, S. M. Lane, and S. Prussin, in *Laser Interaction and Related Plasma Phenomena*, edited by H. Hora and G. H. Miley (Plenum Publishing, New York, 1986), Vol. 7, pp. 421–448.

13. T. J. Kessler, Y. Lin, J. J. Armstrong, and B. Velazquez, in *Laser Coherence Control: Technology and Applications*, edited by H. T. Powell and T. J. Kessler (SPIE, Bellingham, WA, 1993), Vol. 1870, pp. 95–104.

14. T. R. Boehly, V. A. Smalyuk, D. D. Meyerhofer, J. P. Knauer, D. K. Bradley, R. S. Craxton, M. J. Guardalben, S. Skupsky, and T. J. Kessler, J. Appl. Phys. **85**, 3444 (1999).

15. S. Skupsky, R. W. Short, T. Kessler, R. S. Craxton, S. Letzring, and J. M. Soures, J. Appl. Phys. **66**, 3456 (1989).

16. F. J. Marshall, J. A. Delettrez, R. Epstein, R. Forties, V. Yu. Glebov, J. H. Kelly, T. J. Kessler, J. P. Knauer, P. W. McKenty, S. P. Regan, V. A. Smalyuk, C. Stoeckl, J. A. Frenje, C. K. Li, R. D. Petrasso, and F. H. Séguin, Bull. Am. Phys. Soc. **48**, 56 (2003).

17. F. J. Marshall, J. A. Delettrez, R. Epstein, R. Forties, R. L. Keck, J. H. Kelly, P. W. McKenty, S. P. Regan, and L. J. Waxer, Phys. Plasmas **11**, 251 (2004).

18. R. C. Malone, R. L. McCrory, and R. L. Morse, Phys. Rev. Lett. **34**, 721 (1975).

19. J. Delettrez, Can. J. Phys. **64**, 932 (1986).

20. W. Seka, C. Stoeckl, V. N. Goncharov, R. E. Bahr, T. C. Sangster, R. S. Craxton, J. A. Delettrez, A. V. Maximov, J. Myatt, A. Simon, and R. W. Short, Bull. Am. Phys. Soc **49**, 179 (2004).

21. C. Stoeckl, V. Yu. Glebov, S. Roberts, T. C. Sangster, R. A. Lerche, R. L. Griffith, and C. Sorce, Rev. Sci. Instrum. **74**, 1713 (2003).

22. R. D. Petrasso, J. A. Frenje, C. K. Li, F. H. Séguin, J. R. Rygg, B. E. Schwartz, S. Kurebayashi, P. B. Radha, C. Stoeckl, J. M. Soures, J. Delettrez, V. Yu. Glebov, D. D. Meyerhofer, and T. C. Sangster, Phys. Rev. Lett. **90**, 095002 (2003).

23. V. A. Smalyuk, P. B. Radha, J. A. Delettrez, V. Yu. Glebov, V. N. Goncharov, D. D. Meyerhofer, S. P. Regan, S. Roberts, T. C. Sangster, J. M. Soures, C. Stoeckl, J. A. Frenje, C. K. Li, R. D. Petrasso, and F. H. Séguin, Phys. Rev. Lett. **90**, 135002 (2003).

24. J. A. Frenje, C. K. Li, F. H. Séguin, J. Deciantis, S. Kurebayashi, J. R. Rygg, R. D. Petrasso, J. Delettrez, V. Yu. Glebov, C. Stoeckl, F. J. Marshall, D. D. Meyerhofer, T. C. Sangster, V. A. Smalyuk, and J. M. Soures, Phys. Plasmas **11**, 2798 (2003).

25. F. J. Marshall, J. A. Delettrez, R. Epstein, and B. Yaakobi, Phys. Rev. E **49**, 4381 (1994).

26. D. Keller, T. J. B. Collins, J. A. Delettrez, P. W. McKenty, P. B. Radha, B. Whitney, and G. A. Moses, Bull. Am. Phys. Soc. **44**, 37 (1999).